Published in final edited form as:
Concepts Magn Reson Part B Magn Reson Eng. 2011 October ; 39B(4): 206–216. doi:10.1002/cmr.b.20209.

Numerical Analysis of Human Sample Effect on RF Penetration and Liver MR Imaging at Ultrahigh Field

Yong Pang[1], **Bing Wu**[1], **Chunsheng Wang**[1], **Daniel B. Vigneron**[1,2], and **Xiaoliang Zhang**[1,2]

[1]Department of Radiology & Biomedical Imaging, University of California San Francisco, San Francisco, CA

[2]UCSF/UC Berkeley Joint Graduate Group in Bioengineering, San Francisco & Berkeley, CA

Abstract

Magnetic resonance imaging (MRI) can provide clinically-valuable images for hepatic diseases and has become one of the most promising noninvasive methods in evaluating liver lesions. To facilitate the ultrahigh field human liver MRI, in this work, the RF penetration behavior in the conductive and high dielectric human body at the ultrahigh field of 7 Tesla (7T) is investigated and evaluated using the finite-difference time-domain numerical analysis. The study shows that in brain imaging at the ultrahigh field of 7T, the "dielectric resonance" effect dominates among other factors, resulting in improved B_1 penetration; while in liver imaging, due to its irregular geometry of the liver, the "dielectric resonance" effect is not readily to be established, leading to a reduced B_1 penetration or limited image coverage comparing to that in the brain. Therefore, it is necessary to build a large size coil to have deeper penetration to image human liver although the coil design may become more challenging due to the required high frequency. Based on this study, a bisected microstrip coil operating at 300 MHz range is designed and constructed. Three-dimensional in vivo liver images in axial, sagittal and coronal orientations are then acquired from healthy volunteers using this dedicated RF coil on a 7T whole body MR scanner.

Keywords

RF penetration; ultrahigh field; surface coil; MR imaging

I. INTRODUCTION

Magnetic resonance imaging (MRI) has become one of the most promising noninvasive methods in evaluating the liver under normal and diseased conditions (1–9). Clinically-valuable images could be obtained using T1 or T2 weighted imaging techniques, which increase the contrast between normal hepatic parenchyma and liver lesion. The 3D gradient-echo sequence and fast spin-echo sequence (10) have been applied to liver imaging, which achieved higher spatial resolution than that in conventional 2D sequences (1, 2). To accelerate the acquisition, parallel imaging (11–17) has been utilized to reduce the imaging time for both breath-hold sequences and respiratory-triggered sequences for 1.5T liver imaging (9). However, tradeoffs must be made between the signal-to-noise ratio (SNR) and acceleration factor. An effective way to improve the SNR is to use high field MRI because the SNR increases with the field strength. This high SNR advantage has been demonstrated

*Correspondence to: Xiaoliang Zhang; xiaoliang.zhang@ucsf.edu.

by high field in vivo liver imaging and abdominal imaging at 3T, although some artifacts and technical challenges exist (4, 7).

In recent years, high and ultrahigh field such as 7T has shown its inherent ability to improve the SNR (18–27). Human head imaging (28–37), prostate imaging (38, 39), spine imaging (40–42), and liver imaging (43, 44) have been investigated at 7T and have demonstrated high quality images. It is expected that with ultrahigh field liver imaging, better SNR can be achieved so that high resolution images become possible. Moreover, liver images with breath-hold can be acquired using very short echo time (TE), which is able to shorten the scan time and reduce motion artifacts. Furthermore, the susceptibility effect becomes more prominent with the increase of the field strength (45), which makes the detection and quantification of hepatic iron store (46) more effective in susceptibility weighted imaging. These expected advantages make ultrahigh field liver imaging interesting and worthy of investigating.

However, transferring liver protocols to high and ultrahigh fields faces many technical challenges and practical difficulties. The RF penetration in human liver at high frequency becomes more subject to the electromagnetic properties and geometry of the tissue. This problem is more pronounced with the increase of the field strength, presenting great challenges in both RF coil design and sequence design for human liver imaging at high fields. In this study, the finite-difference time-domain (FDTD) method was applied to analyze the RF field penetration behavior of an 8-cm diameter surface coil which is a common coil type used in human magnetic resonance (MR) imaging. Although such sized coils have less design challenges and can be readily designed and constructed using conventional lumped element method for 7T imaging, the numerical study demonstrates that these coils show limitations in imaging coverage and RF penetration in human liver imaging. It is known that increasing coil size can generally enlarge imaging coverage. However, due to the increased inductance and the required high frequency, it is challenging to design large RF coils for ultrahigh field MR applications. To address these technical issues in liver imaging at 7T, a high frequency, large-sized microstrip transceiver coil (47–52) with bisection scheme was designed and constructed for improved MR signal excitation and reception. Using the microstrip coil, preliminary in vivo liver images were acquired from healthy volunteers using a steady state free precession (SSFP) sequence on a whole body 7T MR scanner.

II. MATERIALS AND METHODS

Evaluation of Surface Coil Penetration for Human Liver and Brain at 300 MHz

Surface coils have high SNR in the area near the coil; however, the SNR decreases with the increase of the distance away from the coil. Therefore, the coil penetration, which describes the available SNR at a deep distance, becomes an important issue in evaluating the coil performance. In human imaging studies, different human body tissues have different geometries and electromagnetic properties, leading to different RF field distribution when using the same coil. At high and ultrahigh fields, the RF shielding effect may become a factor, which affects the RF field penetration into the conductive human body. The shielding effect in homogeneous samples can be theoretically described by the skin depth:

$$\delta = \sqrt{\frac{2}{\omega\mu\sigma}} \quad (1)$$

where the ω, μ, σ denote the angular frequency, permeability constant, and conductivity constant respectively. This equation shows that the RF penetration inside a conductive

sample is inversely proportional to the square root of the sample conductivity and the operation frequency. It is worth noting that the behavior on skin depth of the heterogenous human tissues is more complicated than the homogeneous materials. Although Eq. [1] (which is more accurate for good conductors) can reflect the shielding effect for conductive materials/tissues, it may not be able to give a quantitatively meaningful result of RF field penetration in human tissues due to the complexity of heterogeneous tissues and their surrounding environment. Another factor which affects the RF field distribution in a sample is the so-called “dielectric resonance” effect. When a dielectric sample has a regular geometry (e.g., sphere, cube, cylinder, rectangular cuboid, etc.) and its size is finite and comparable or bigger than the wavelength of the operation frequency, the dielectric resonance may be established in the sample. At ultrahigh fields, due to the high operation frequency, the wavelength of the RF field usually becomes comparable with the size of human body or organs. It is possible to establish “dielectric resonance” at certain degree in high permittivity human samples if their geometry is regular or close to regular. This “dielectric resonance” effect usually helps improve the RF penetration (53). To investigate the image coverage and penetration behavior in liver imaging at 7T, numerical simulations using FDTD method was performed to a surface coil with a high fidelity human whole body model. Conventionally, bigger coils have deeper B_1 penetration and image coverage. The numerical calculations of the B_1 field distributions of the RF coil model would be used to guide the design and construction of the surface coil for the liver imaging in this work.

The software XFDTD6.4 (Remcom, State College) was used in the simulation studies. The high fidelity human model provides detailed tissue structure in human head and abdomen, including skin, yellow marrow, cortical bone, white matter, gray matter, CSF, fat, blood vessel, and liver. The surface coil was modeled as a copper loop with 8 cm O.D. (outer diameter) and 7 cm I.D. (inner diameter). The selection of the coil size for the calculation model was based on our imaging experience at ultrahigh field of 7T. Surface coils with 8-cm diameter or less resonating at 300 MHz can be realized in a conventional approach without a significant design effort. Two typical human samples—liver and brain—were used in the simulation for comparison. Both liver and brain have similar conductivity, however, the liver has an irregular geometry and relatively low permittivity while the brain has a comparatively regular geometry and high permittivity (At 300 MHz, relative permittivity of White matter: 43.8; Gray matter: 60; CSF: 72.7; Liver: 53.5). In the human liver simulation, the coil model was placed above the liver and ~ 1 cm away from the abdomen, as shown in Figures 1(a,c,e). In the human brain simulation, this coil model was placed behind the occipital lobe and also ~ 1 cm away from the head, as shown in Figures 1(b,d,f). A current source was utilized to generate a 300 MHz alternating current to ensure the RF pulse was at 300 MHz. The stop criteria for FDTD calculation is convergence to −40 dB. For both liver and brain, transmission field B_1+ and reception field B_1- distributions were both simulated and the signal intensity was calculated using the following equation (54):

$$I \propto \sum_{N} \left| W_n \sin(V \left| B_{1n}^{+} \right| \gamma\tau) \left| (B_{1n}^{-})^{*} \right| \right| \tag{2}$$

where N is the total number of the voxels within the field of view (FOV); $B_{1n}+$ and $B_{1n}-$ denote the transmission field and reception field, respectively; γ denotes the gyromagnetic ratio. W_n is the water content percentage of the nth voxel, and t is the excitation duration. V is a normalization factor which is used to achieve the maximum signal at the nearest position to the coil within the human body.

Microstrip Surface Coil Design

Based on the simulation analysis, it is necessary to build a large size coil to have deeper penetration to image human liver although the design may face significant technical challenges due to the required high frequency. A bisected microstrip surface coil was built to detect the MR signal of human liver. As shown in Figure 2, the microstrip coil is circular shaped with 12.5cm ID, 15.3cm OD, and 1.4 cm strip width. On one end of the coil a capacitor (Dalicap, Dalian, China) with nominal capacitance of 2.7 pF was used as termination. On the other end a variable capacitor (Voltronics, NMAP25HV) ranging from 1 to 25 pF acted as tuning capacitor. A fixed capacitor of 2.7 pF (Dalicap, Co) was used to couple the two microstrip resonators. A nonmagnetic trimmer capacitor (Voltronics, NMAP19HV) ranging from 1 to 19 pF served as impedance matching. The circular strip conductor was built on the top of a square-shaped Teflon substrate with a relative low permittivity of 2.1 and low loss-tangent of 0.0002, side length of 20 cm and thickness of half inch. The relatively thick substrate of half inch is necessary to help increase the B_1 penetration so that the deep region of the liver can be imaged. The ground plane of the coil was a single piece copper adhering to the bottom of the substrate. Bench test of this coil was performed on an Agilent network analyzer.

Pulse Sequence and Imaging Parameters

In vivo experiments were performed on a GE whole body 7T scanner with maximum gradient strength of 4 Gauss/cm and maximum slew rate of 15 Gauss/cm/ms. The subject position was supine, entry was foot first and the surface coil was placed on the upright position of liver. A SSFP sequence was used for imaging axial, sagittal and coronal slices of human liver. For the axial and sagittal images, the imaging parameters were: Receiver bandwidth = 31.25 kHz, FOV = 20 cm, slice thickness = 5 mm, slice spacing = 3 mm, matrix = 256 × 128, phase FOV = 1, flip angle = 30°, TR = 5 ms and TE = 1.32 ms, and number of excitation = 1. For the coronal images, Receiver bandwidth = 23.4 kHz, FOV = 20cm, slice thickness = 5 mm, slice spacing = 3 mm, matrix = 384 × 256, phase FOV = 1, flip angle = 30°, TR = 6 ms, TE = 1.64 ms, and number of excitation = 2. The phase encoding direction is superior–inferior.

III. RESULTS

Simulation of Coil Penetration in Human Liver and Brain

B_1+ and B_1- field distributions of both human liver and brain were simulated using the FDTD method. The signal intensity of both the axial plane and sagittal plane were calculated using the Eq. [2]. Figure 3(a,b) show the 2D signal intensity of the axial planes of the liver and brain respectively. Figure 3(c) is their corresponding 1D plot of the signal intensity along the dashed line indicated in Figure 3(a,b). At 10 cm away, the signal intensity decreased to 8.8% in human brain phantom while decreased to 0.7% in liver phantom. It clearly demonstrated that using the same 8 cm O.D. surface coil, the B_1 penetration was fairly different when applied to different imaging objects. In the human liver whose geometry was irregular, not close to any regular shapes that dielectric resonators usually have, the dielectric resonance is not easy to be established. In the human brain that has a comparatively regular geometry and high permittivity, dielectric resonance tends to happen, helping improve the B_1 field penetration.

Figure 4 shows the 2D views and 1D plots of the liver and brain signal intensity in the sagittal plane. It is shown that at 10 cm away, the signal intensity decreases to 9.4% in the brain phantom and to 0.7% in liver phantom. The obvious penetration difference again demonstrated that different body tissues have different effects on coil penetration. Therefore, it is necessary to design a coil with sufficient B_1 penetration and image coverage to achieve

a good human liver image at 7 Tesla. Based on the simulated B_1 distribution of an 8-cm surface coil in the liver shown in Figures 3 and 4, a coil with doubled diameter would be needed to provide reasonable image coverage in liver imaging at 7T.

Bench Test of the Coil Performance

Based on the simulation and experience, a microstrip surface coil with 15.3 cm O.D. was built for human liver imaging. The bench test result is shown in Figure 5. At 298.2 MHz, the S_{11} parameter in the loaded case was able to reach −50 dB, showing excellent impedance match. The unloaded and loaded Q factors were 330 and 40, respectively. This high Q ratio indicates excellent coil loading efficiency. To reach deep penetration, a thick dielectric substrate of 1/2 inch was used; therefore in the loaded case most power was delivered into human body. By varying the capacitance of the tuning capacitor, the maximum and minimum frequency could reach 315.3 and 230.5 MHz, respectively. This large frequency tuning range of approximate 85 MHz would be very helpful in practice.

In Vivo Study of Human Liver

Axial, sagittal and coronal images of human liver were obtained using a SSFP sequence and each imaging set was performed within a breath-hold with an acquisition time of up to 23 s. The images are shown in Figures 6, 7, and 8, respectively. It can be seen that the coil has a large penetration and nearly all the liver is covered. The image intensity decay profile on each axial slice in Figure 6 was also plotted to illustrate the RF field attenuation with depth to the coil. The simulation result of a 15.3 cm OD surface coil was also plotted in Figure 6(a) for comparison. It is shown that the image intensity decay profile of the simulated result is similar to that of the MR images. Compared with Figure 3, the RF penetration was obviously improved as expected. The SNR of each coronal slice is shown in Table 1. At ultrahigh field the B_1 variation and susceptibility become more pronounced, causing slight frequency shifts within FOV. This off-resonance leads to some banding artifacts on the liver images.

IV. DISCUSSION AND CONCLUSIONS

The feasibility of human liver imaging at 7T was investigated through theoretical analysis and in vivo imaging experiments. The RF field penetration was investigated using the FDTD method for an 8-cm surface coil, that is, a commonly-used coil type in human MRI. It was shown that in human liver imaging at 7T, to achieve the same RF penetration as that in the head at the same field strength the coil size should be larger than that used for head imaging to compensate for the reduced RF penetration due to less dielectric resonance effect in the liver. On the other hand, a large RF coil is potentially to decrease the achievable SNR. Therefore, tradeoffs must be made to compromise between the image coverage and the SNR. In our in vivo MRI experiments, a large size surface coil with 15.3 cm diameter using microstrip technique was built and a SSFP sequence was utilized to acquire in vivo images of human liver.

With the increased magnetic field strength, the effect of human body on the RF penetration and image coverage becomes more obvious. From the FDTD simulation results, it was observed that this effect in the liver and the brain is significantly different from each other. In the liver which has relatively irregular geometry, the “dielectric resonance” is not easy to be established to help the field penetration at ultrahigh frequency such as 300 MHz in this application. This effect will restrict the detectable signals from the deep region of the subjects, significantly decreasing the achievable coil penetration. In the brain, which has relatively regular geometry (close to a sphere) and high permittivity, the dielectric resonance becomes dominant at the ultrahigh frequency. This dielectric resonance mode helps to

increase the SNR of the area far from the coil, leading to improved coil penetration. This is part of the reason that at ultrahigh fields, B_1 generated by RF coils have good penetration in brain imaging (53) while liver imaging usually suffers from the imaging coverage and penetration problems (7).

In human liver imaging at ultrahigh fields, due to the requirement of large image coverage and penetration, design of an efficient, large-sized RF coil operating at high frequency is essential. The numerical calculation results suggest that an approximate 15-cm coil would be required for human liver imaging at 7T. To build such a large surface coil with practical frequency tuning capability for optimization of resonant frequency in different loading, microstrip transmission line technique is more suitable than conventional lumped element technique due to its proven advantages in high frequency capability, high Q factors and broad frequency tuning range. Conventional lumped element design with split capacitors shows technical difficulties and limitations to achieve the required high resonant frequency and reasonable frequency tuning range in designing large size coils for 7T imaging. In the proposed bisected microstrip surface coil design, the resonant frequency of this 15-cm coil can readily achieve to the required 300 MHz range, and the frequency tuning range could reach 85 MHz (from 230.5 to 315.3 MHz). Also, at 298.2 MHz, the Q factor can reach 40 in the fully loaded case. The ratio of unloaded Q to loaded Q was better than 8, demonstrating excellent loading efficiency.

By using the proposed bisected microstrip transceiver surface coil, preliminary study in human liver imaging was investigated with the SSFP sequence at 7T. Axial, sagittal and coronal images show that the coil has a good coverage in human liver imaging. With breath holding, the motion artifacts were greatly reduced. This experiment demonstrated the feasibility of human liver imaging at the ultrahigh field of 7T. Further investigations with higher spatial resolution using optimized imaging parameters and sequences are now being pursued.

Acknowledgments

This work was partially supported by NIH grants EB004453, EB008699, EB007588-03S1, and P41 EB013598, and a QB3 Research Award. The authors thank Mihir Pendse for manuscript editing and proofreading.

REFERENCES

1. Hennig J, Weigel M, Scheffler K. Multiecho sequences with variable refocusing flip angles: optimization of signal behavior using smooth transitions between pseudo steady states (TRAPS). Magn Reson Med. 2003; 49:527–535. [PubMed: 12594756]
2. Lee VS, Lavelle MT, Rofsky NM, Laub G, Thomasson DM, Krinsky GA, et al. Hepatic MR imaging with a dynamic contrast-enhanced isotropic volumetric interpolated breath-hold examination: feasibility, reproducibility, and technical quality. Radiology. 2000; 215:365–372. [PubMed: 10796909]
3. McFarland EG, Mayo-Smith WW, Saini S, Hahn PF, Goldberg MA, Lee MJ. Hepatic hemangiomas and malignant tumors: improved differentiation with heavily T2-weighted conventional spin-echo MR imaging. Radiology. 1994; 193:43–47. [PubMed: 8090920]
4. Merkle EM, Dale BM, Paulson EK. Abdominal MR imaging at 3T. Magn Reson Imaging Clin N Am. 2006; 14:17–26. [PubMed: 16530632]
5. Mitchell DG, Saini S, Weinreb J, De Lange EE, Runge VM, Kuhlman JE, et al. Hepatic metastases and cavernous hemangiomas: distinction with standard- and triple-dose gadoteridol-enhanced MR imaging. Radiology. 1994; 193:49–57. [PubMed: 8090921]
6. Mortele KJ, Praet M, Van Vlierberghe H, Kunnen M, Ros PR. CT and MR imaging findings in focal nodular hyperplasia of the liver: radiologic-pathologic correlation. AJR Am J Roentgenol. 2000; 175:687–692. [PubMed: 10954451]

7. Ramalho M, Altun E, Heredia V, Zapparoli M, Semelka R. Liver MR imaging: 1.5T versus 3T. Magn Reson Imaging Clin N Am. 2007; 15:321–347. vi. [PubMed: 17893053]
8. Smith FW, Mallard JR, Reid A, Hutchison JM. Nuclear magnetic resonance tomographic imaging in liver disease. Lancet. 1981; 1(8227):963–966. [PubMed: 6112385]
9. Zech CJ, Herrmann KA, Huber A, Dietrich O, Stemmer A, Herzog P, et al. High-resolution MR-imaging of the liver with T2-weighted sequences using integrated parallel imaging: comparison of prospective motion correction and respiratory triggering. J Magn Reson Imaging. 2004; 20:443–450. [PubMed: 15332252]
10. Yuan J, Zhao TC, Tang Y, Panych LP. Reduced field-of-view single-shot fast spin echo imaging using two-dimensional spatially selective radiofrequency pulses. J Magn Reson Imaging. 2010; 32:242–248. [PubMed: 20578031]
11. Griswold MA, Jakob PM, Heidemann RM, Nittka M, Jellus V, Wang J, et al. Generalized autocalibrating partially parallel acquisitions (GRAPPA). Magn Reson Med. 2002; 47:1202–1210. [PubMed: 12111967]
12. Qu P, Shen GX, Wang C, Wu B, Yuan J. Tailored utilization of acquired k-space points for GRAPPA reconstruction. J Magn Reson. 2005; 174:60–67. [PubMed: 15809173]
13. Ying, L.; Haldar, J.; Liang, ZP. An efficient non-iterative reconstruction algorithm for parallel MRI with arbitrary k-space trajectories; Conf Proc IEEE Eng Med Biol Soc; 2005. p. 1344-1347.
14. Ying, L.; Xu, D.; Liang, ZP. On Tikhonov regularization for image reconstruction in parallel MRI; Conf Proc IEEE Eng Med Biol Soc; 2004. p. 1056-1059.
15. Pruessmann KP, Weiger M, Scheidegger MB, Boesiger P. SENSE: sensitivity encoding for fast MRI. Magn Reson Med. 1999; 42:952–962. [PubMed: 10542355]
16. Sodickson DK, Manning WJ. Simultaneous acquisition of spatial harmonics (SMASH): fast imaging with radiofrequency coil arrays. Magn Reson Med. 1997; 38:591–603. [PubMed: 9324327]
17. Lee JH, Scott GC, Pauly JM, Nishimura DG. Broadband multicoil imaging using multiple demodulation hardware: a feasibility study. Magn Reson Med. 2005; 54:669–676. [PubMed: 16086362]
18. Pang Y, Zhang X, Xie Z, Wang C, Vigneron D. Common-mode differential-mode (CMDM) method for double-nuclear MR signal excitation and reception at ultrahigh fields. IEEE Trans Med Imaging. 2011 Epub ahead of print, 2011 Jun 20,
19. Shen GX, Wu JF, Boada FE, Thulborn KR. Experimentally verified, theoretical design of dual-tuned, low-pass birdcage radiofrequency resonators for magnetic resonance imaging and magnetic resonance spectroscopy of human brain at 3.0 Tesla. Magn Reson Med. 1999; 41:268–275. [PubMed: 10080273]
20. Wiggins GC, Potthast A, Triantafyllou C, Wiggins CJ, Wald LL. Eight-channel phased array coil and detunable TEM volume coil for 7 T brain imaging. Magn Reson Med. 2005; 54:235–240. [PubMed: 15968650]
21. Zelinski AC, Angelone LM, Goyal VK, Bonmassar G, Adalsteinsson E, Wald LL. Specific absorption rate studies of the parallel transmission of inner-volume excitations at 7T. J Magn Reson Imaging. 2008; 28:1005–1018. [PubMed: 18821601]
22. Yacoub E, Shmuel A, Pfeuffer J, Van De Moortele PF, Adriany G, Ugurbil K, et al. Investigation of the initial dip in fMRI at 7 Tesla. NMR Biomed. 2001; 14:408–412. [PubMed: 11746933]
23. Yacoub E, Van De Moortele PF, Shmuel A, Ugurbil K. Signal and noise characteristics of Hahn SE and GE BOLD fMRI at 7 T in humans. Neuroimage. 2005; 24:738–750. [PubMed: 15652309]
24. Lei H, Zhang Y, Zhu XH, Chen W. Changes in the proton T2 relaxation times of cerebral water and metabolites during forebrain ischemia in rat at 9.4 T. Magn Reson Med. 2003; 49:979–984. [PubMed: 12768573]
25. Lei H, Zhu XH, Zhang XL, Ugurbil K, Chen W. In vivo 31P magnetic resonance spectroscopy of human brain at 7 T: an initial experience. Magn Reson Med. 2003; 49:199–205. [PubMed: 12541238]
26. Pang Y, Xie Z, Li Y, Xu D, Vigneron D, Zhang X. Resonant mode reduction in radiofrequency volume coils for ultrahigh field magnetic resonance imaging. Materials. 2011; 4:1333–1344. [PubMed: 22081791]

27. Li Y, Xie Z, Pang Y, Vigneron D, Zhang X. ICE decoupling technique for RF coil array designs. Med Phys. 2011; 38:4086–4093. [PubMed: 21859008]
28. Vaughan JT, Garwood M, Collins CM, Liu W, Dela-Barre L, Adriany G, et al. 7T vs. 4T: RF power, homogeneity, and signal-to-noise comparison in head images. Magn Reson Med. 2001; 46:24–30. [PubMed: 11443707]
29. Avdievich NI, Hetherington HP, Kuznetsov AM, Pan JW. 7T head volume coils: improvements for rostral brain imaging. J Magn Reson Imaging. 2009; 29:461–465. [PubMed: 19161203]
30. Avdievich NI, Pan JW, Baehring JM, Spencer DD, Hetherington HP. Short echo spectroscopic imaging of the human brain at 7T using transceiver arrays. Magn Reson Med. 2009; 62:17–25. [PubMed: 19365851]
31. Choi C, Dimitrov IE, Douglas D, Patel A, Kaiser LG, Amezcua CA, et al. Improvement of resolution for brain coupled metabolites by optimized (1)H MRS at 7T. NMR Biomed. 2010; 23:1044–1052. [PubMed: 20963800]
32. Eapen M, Zald DH, Gatenby JC, Ding Z, Gore JC. Using High-Resolution MR Imaging at 7T to Evaluate the Anatomy of the Midbrain Dopaminergic System. AJNR Am J Neuroradiol. 2011; 32:688–694. [PubMed: 21183619]
33. Fukunaga M, Li TQ, van Gelderen P, de Zwart JA, Shmueli K, Yao B, et al. Layer-specific variation of iron content in cerebral cortex as a source of MRI contrast. Proc Natl Acad Sci U S A. 2010; 107:3834–3839. [PubMed: 20133720]
34. Li TQ, Yao B, van Gelderen P, Merkle H, Dodd S, Talagala L, et al. Characterization of T(2)* heterogeneity in human brain white matter. Magn Reson Med. 2009; 62:1652–1657. [PubMed: 19859939]
35. Liu S, Gonen O, Fleysher L, Fleysher R, Soher BJ, Pilkenton S, et al. Regional metabolite T2 in the healthy rhesus macaque brain at 7T. Magn Reson Med. 2008; 59:1165–1169. [PubMed: 18429024]
36. Qian Y, Zhao T, Hue YK, Ibrahim TS, Boada FE. High-resolution spiral imaging on a whole-body 7T scanner with minimized image blurring. Magn Reson Med. 2010; 63:543–552. [PubMed: 20146226]
37. Yankeelov TE, DeBusk LM, Billheimer DD, Luci JJ, Lin PC, Price RR, et al. Repeatability of a reference region model for analysis of murine DCE-MRI data at 7T. J Magn Reson Imaging. 2006; 24:1140–1147. [PubMed: 17024660]
38. Metzger GJ, Snyder C, Akgun C, Vaughan T, Ugurbil K, Van de Moortele PF. Local B1+ shimming for prostate imaging with transceiver arrays at 7T based on subject-dependent transmit phase measurements. Magn Reson Med. 2008; 59:396–409. [PubMed: 18228604]
39. van den Bergen B, Klomp DW, Raaijmakers AJ, de Castro CA, Boer VO, Kroeze H, et al. Uniform prostate imaging and spectroscopy at 7 T: comparison between a microstrip array and an endorectal coil. NMR Biomed. 2010
40. Wu B, Wang C, Krug R, Kelley DA, Xu D, Pang Y, et al. 7T human spine imaging arrays with adjustable inductive decoupling. IEEE Trans Biomed Eng. 2010; 57:397–403. [PubMed: 19709956]
41. Kraff O, Bitz AK, Kruszona S, Orzada S, Schaefer LC, Theysohn JM, et al. An eight-channel phased array RF coil for spine MR imaging at 7 T. Invest Radiol. 2009; 44:734–740. [PubMed: 19809342]
42. Wu B, Wang C, Lu J, Pang Y, Nelson S, Vigneron D, et al. Multi-channel microstrip transceiver arrays using harmonics for high field MR imaging in humans. IEEE Trans Med Imaging. 2011 Epub ahead of print, 2011 Aug 25,
43. Pang, Y.; Wu, B.; Wang, C.; Vigneron, D.; Zhang, X. 7T human liver imaging using microstrip surface coil; Proceedings of the 18th Annual Meeting of ISMRM; Stockholm. 2010. p. 2587
44. Vaughan JT, Snyder CJ, DelaBarre LJ, Bolan PJ, Tian J, Bolinger L, et al. Whole-body imaging at 7T: preliminary results. Magn Reson Med. 2009; 61:244–248. [PubMed: 19097214]
45. Haacke EM, Mittal S, Wu Z, Neelavalli J, Cheng YC. Susceptibility-weighted imaging: technical aspects and clinical applications, part 1. AJNR Am J Neuroradiol. 2009; 30:19–30. [PubMed: 19039041]

46. Gandon Y, Olivie D, Guyader D, Aube C, Oberti F, Sebille V, et al. Non-invasive assessment of hepatic iron stores by MRI. Lancet. 2004; 363:357–362. [PubMed: 15070565]
47. Lee RF, Westgate CR, Weiss RG, Newman DC, Bottomley PA. Planar strip array (PSA) for MRI. Magn Reson Med. 2001; 45:673–683. [PubMed: 11283996]
48. Zhang X, Ugurbil K, Chen W. Microstrip RF surface coil design for extremely high-field MRI and spectroscopy. Magn Reson Med. 2001; 46:443–450. [PubMed: 11550234]
49. Zhang X, Ugurbil K, Chen W. A microstrip transmission line volume coil for human head MR imaging at 4T. J Magn Reson. 2003; 161:242–251. [PubMed: 12713976]
50. Zhang X, Ugurbil K, Sainati R, Chen W. An inverted-microstrip resonator for human head proton MR imaging at 7 tesla. IEEE Trans Biomed Eng. 2005; 52:495–504. [PubMed: 15759580]
51. Zhang X, Zhu XH, Chen W. Higher-order harmonic transmission-line RF coil design for MR applications. Magn Reson Med. 2005; 53:1234–1239. [PubMed: 15844152]
52. Wu B, Wang C, Kelley DA, Xu D, Vigneron DB, Nelson SJ, et al. Shielded microstrip array for 7T human MR imaging. IEEE Trans Med Imaging. 2010; 29:179–184. [PubMed: 19822470]
53. Adriany G, Van de Moortele PF, Wiesinger F, Moeller S, Strupp JP, Andersen P, et al. Transmit and receive transmission line arrays for 7 Tesla parallel imaging. Magn Reson Med. 2005; 53:434–445. [PubMed: 15678527]
54. Collins CM, Smith MB. Signal-to-noise ratio and absorbed power as functions of main magnetic field strength, and definition of “90 degrees” RF pulse for the head in the birdcage coil. Magn Reson Med. 2001; 45:684–691. [PubMed: 11283997]

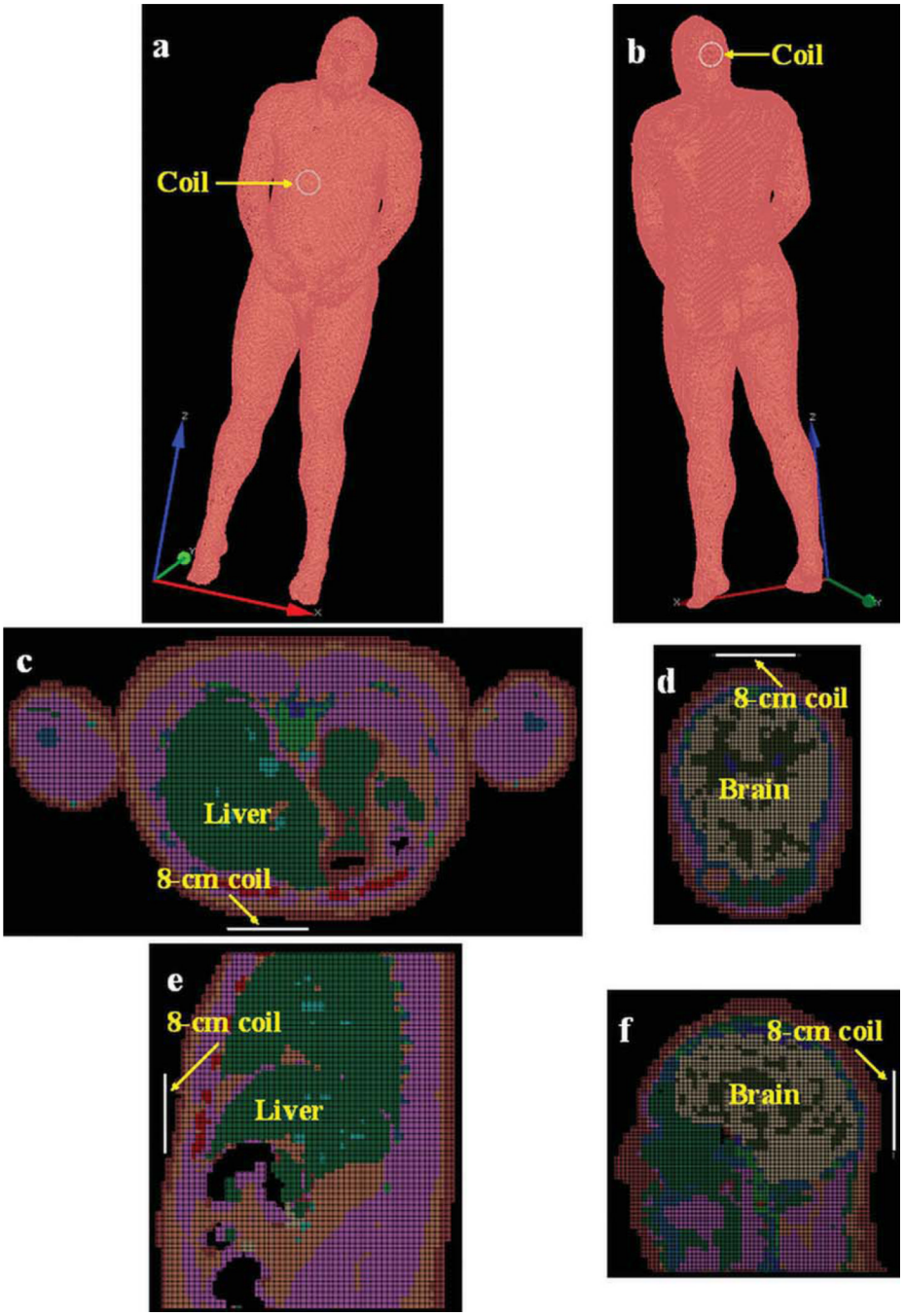

Figure 1.
XFDTD setup for RF penetration comparison between human liver and brain: (a) 3D view of human liver; (b) 3D view of brain; (c) axial plane of liver; (d) axial plane of brain; (e) sagittal plane of liver; (f) sagittal plane of brain.

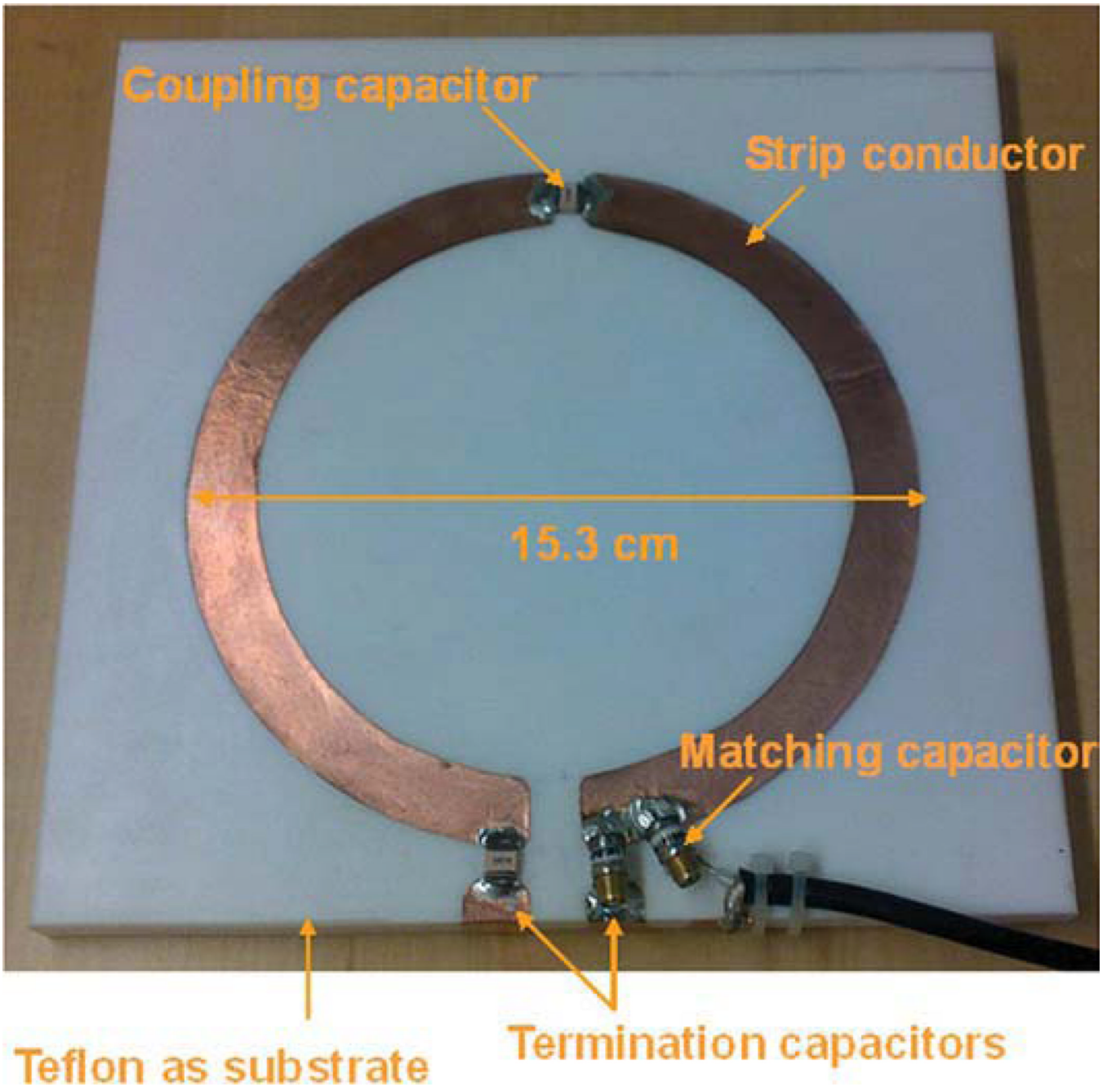

Figure 2.
Prototype of the capacitor terminated bisected microstrip surface coil for human liver imaging at 7T. The bisection microstrip design helps increase the high frequency operation capability for such a large-sized RF coil.

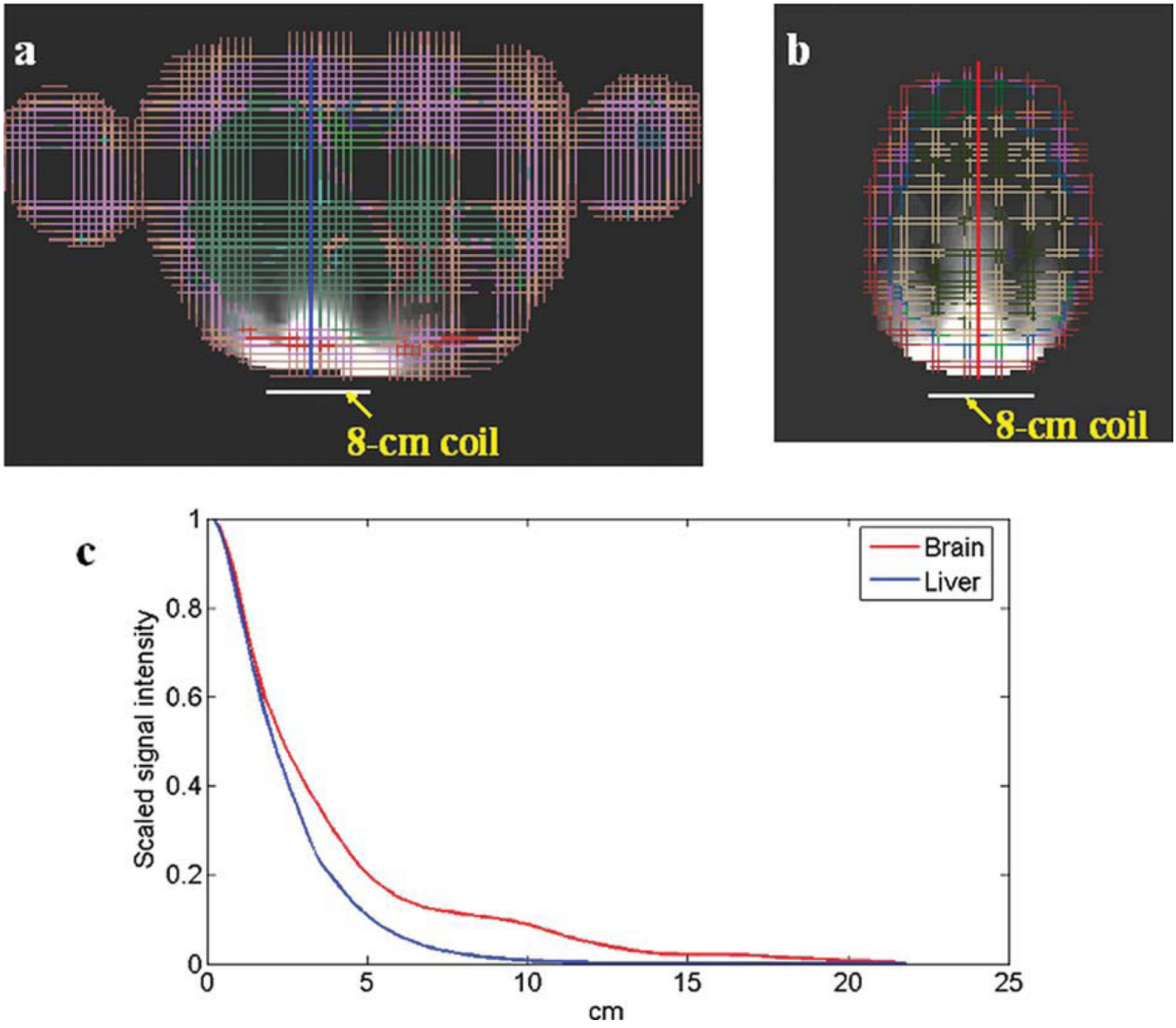

Figure 3.

Simulation results of (a) 2D liver image and (b) 2D brain image of axial plane; (c) 1D plot demonstrates the penetration of corresponding liver and brain images using the size same coil. The geometry of the human liver is irregular, leading to apparent conductivity effect which blocks the RF penetration; while the human brain is with comparatively regular geometry and high permittivity, resulting in obvious dielectric resonance effect which helps improve the RF penetration into the brain.

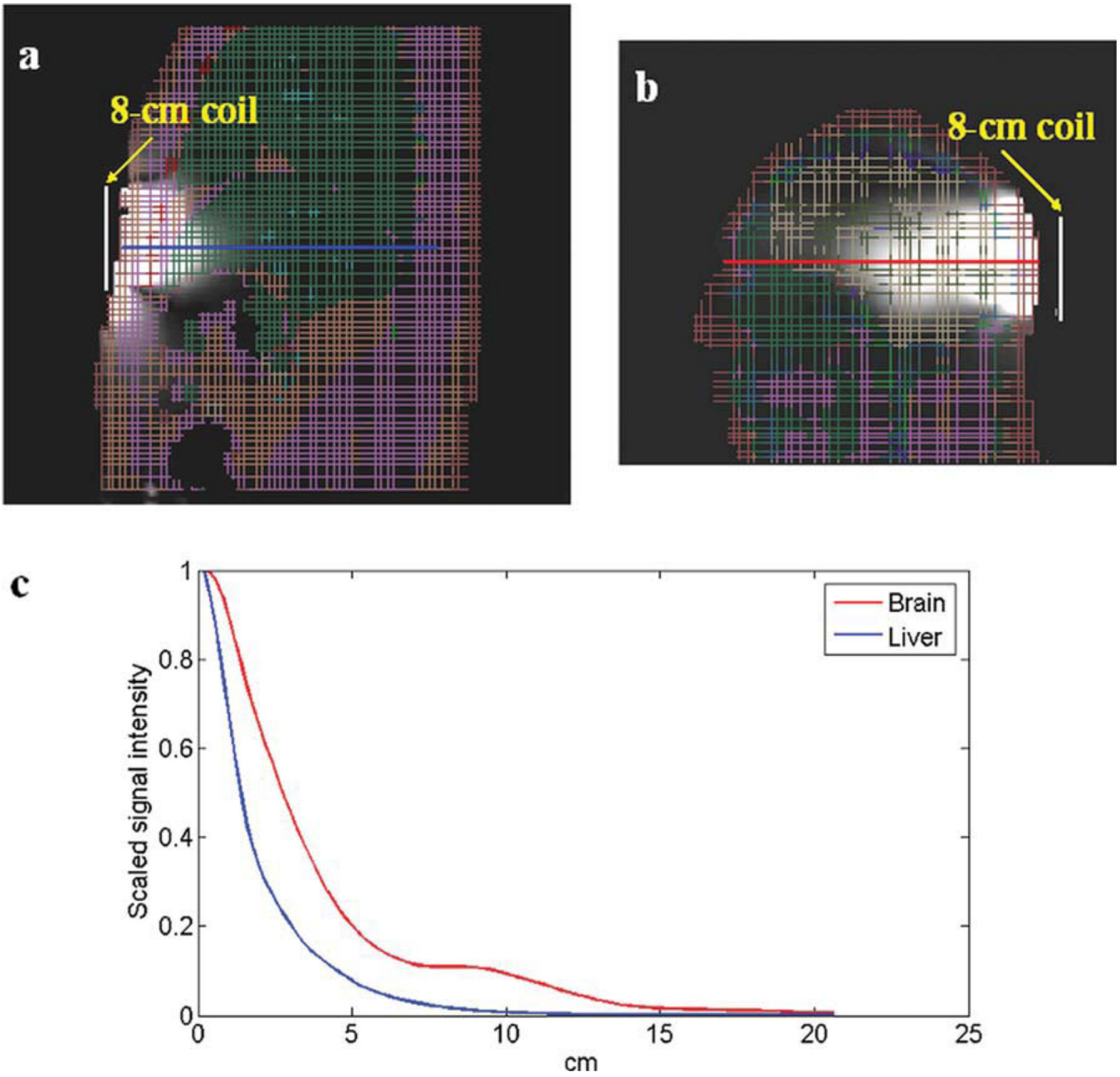

Figure 4.

Simulation results of (a) liver image and (b) brain image of sagittal plane; (c) corresponding 1D plots show the penetration difference between liver and brain using the same size coil. As illustrated in axial images, a deeper RF penetration in the brain is observed than that in the liver.

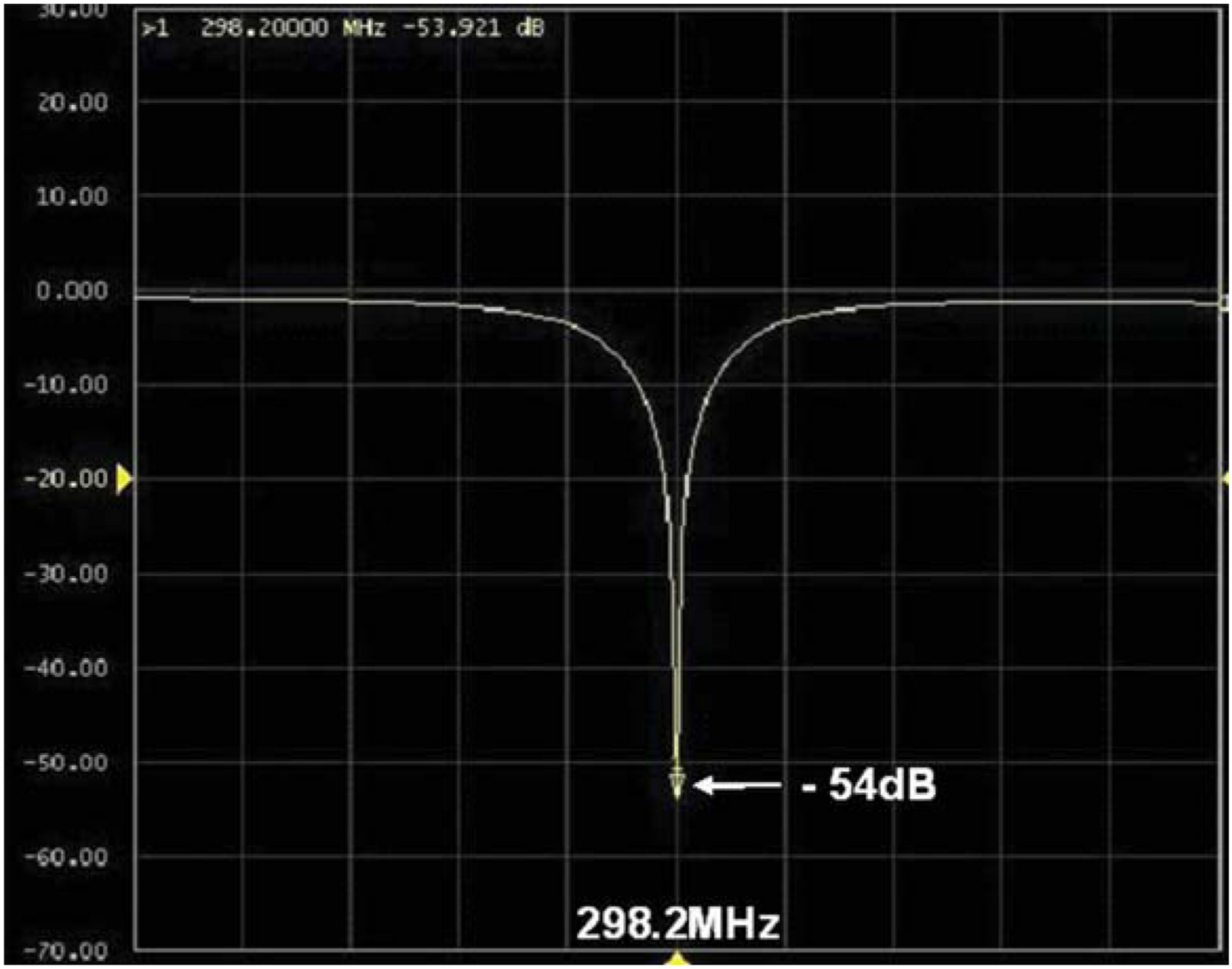

Figure 5.
Bench test of S11 parameter of the proposed bisected microstrip surface coil: At 298.2 MHz (proton Larmor frequency of our whole body 7T MR system), S11 could reach −54dB or better, demonstrating the excellent impedance matching.

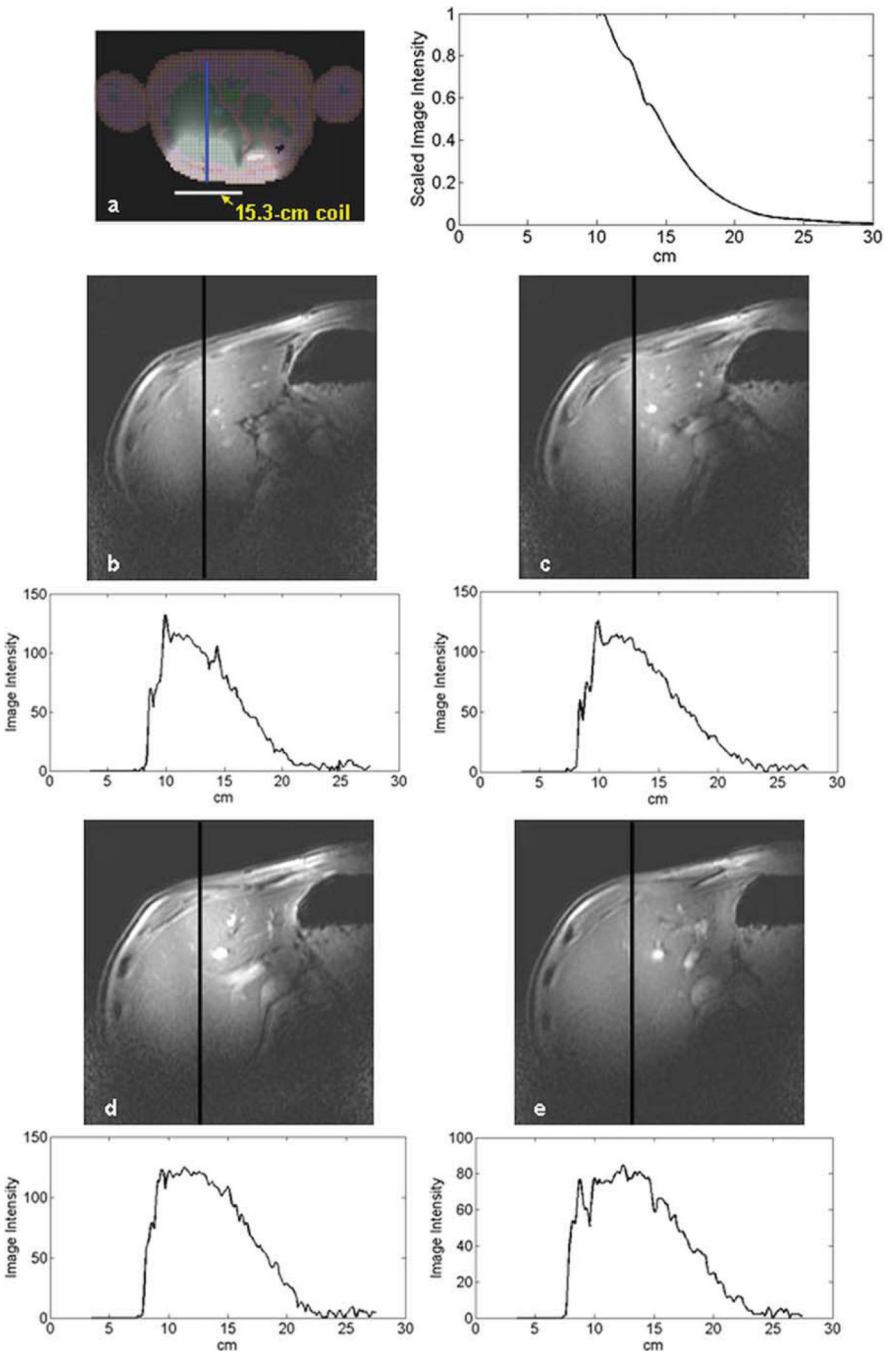

Figure 6.

(a) The simulated B1 penetration of a 15.3 cm surface coil shows similar signal intensity decay profile as those from the MR images. Compared with Fig.3, the RF penetration was obviously improved as expected. (b, c, d, e) 4 axial slices of healthy human liver at different positions using the SSFP sequence. Imaging parameters: bandwidth = 31.25 kHz, FOV = 20cm, slice thickness = 5 mm, slice spacing = 3 mm, matrix = 256 × 128, phase FOV = 1, flip angle = 30°, TR = 5 ms and TE = 1.32 ms, and number of excitation = 1. The 1D image intensity decay profile on each axial slice was also plotted along the line across the MR image to illustrate the RF field attenuation.

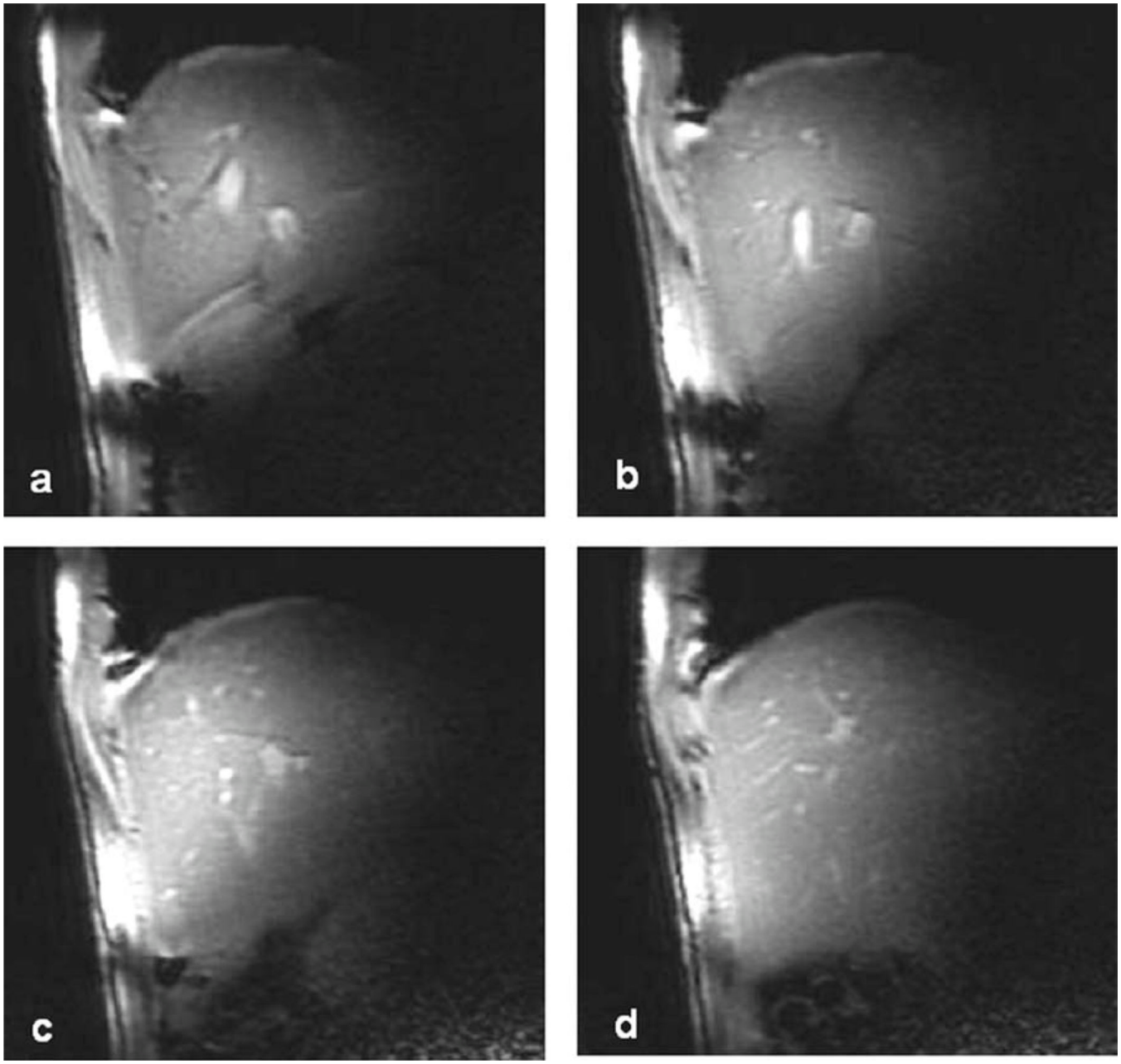

Figure 7.
4 sagittal slices of healthy human liver at different positions using the SSFP sequence. Imaging parameters: bandwidth = 31.25 kHz, FOV = 20cm, slice thickness = 5 mm, slice spacing = 3 mm, matrix = 256 × 128, phase FOV = 1, flip angle = 30°, TR = 5 ms and TE = 1.32 ms, and number of excitation = 1.

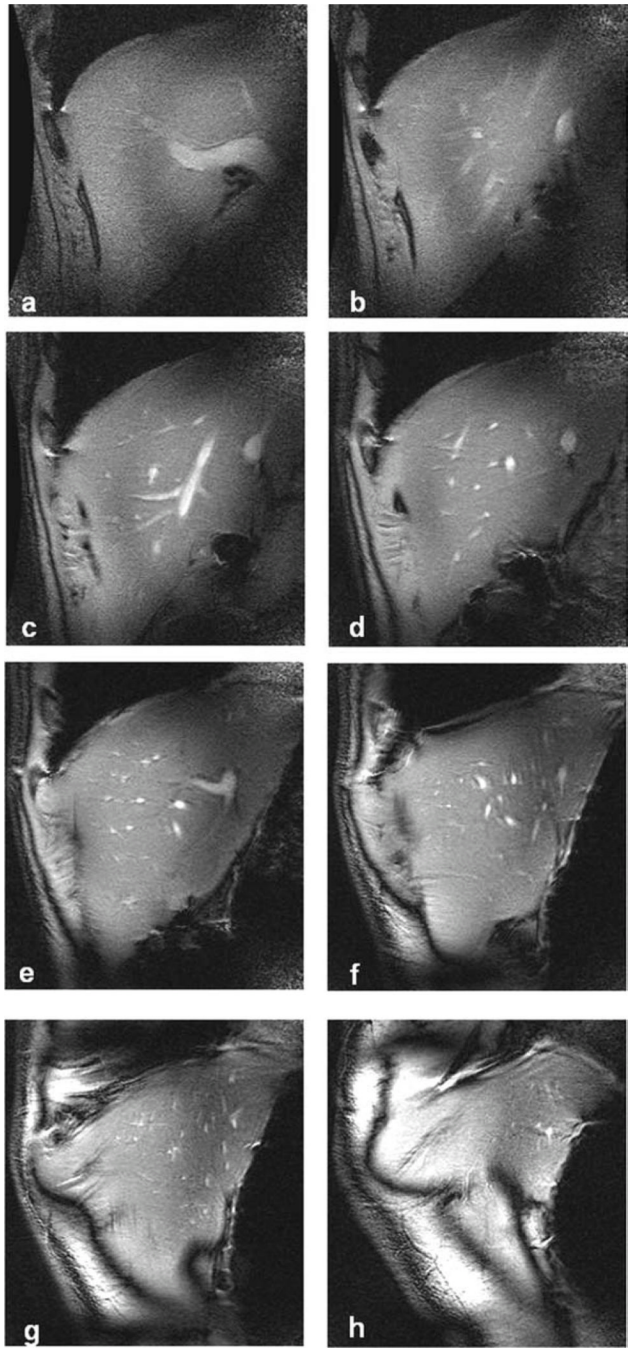

Figure 8.
8 coronal slices of healthy human liver at different positions (superior 5. 5 mm to 61. 5 mm) using the SSFP sequence. Imaging parameters: bandwidth = 23.4 kHz, FOV = 20 cm, slice thickness = 5 mm, slice spacing = 3 mm, matrix = 384 × 256, phase FOV = 1, flip angle = 30°, TR = 6 ms and TE = 1.64 ms, and number of excitation = 2.

Table 1

Average SNR of Each Image of Healthy Human Liver at Different Coronal Slices

Slice	***a***	***b***	***c***	***d***	***e***	***f***	***g***	***h***
Superior (mm)	5.5	13.5	21.5	29.5	37.5	45.5	53.5	61.5
SNR	33.4	36.6	61.3	51.6	59.4	63.5	78.8	96.1

Concepts Magn Reson Part B Magn Reson Eng. Author manuscript; available in PMC 2012 October 1.